Atomistic description of the electronic structure of $In_xGa_{1-x}As$ alloys and InAs/GaAs superlattices

Kwiseon Kim, P. R. C. Kent, and Alex Zunger
National Renewable Energy Laboratory, Golden, Colorado 80401

C. B. Geller
Bettis Atomic Power Laboratory, West Mifflin, Pennsylvania 15122

(Received 12 March 2002; published 30 July 2002)

We show how an empirical pseudopotential approach, fitted to bulk and interfacial reference systems, provides a unified description of the electronic structure of random alloys (bulk and epitaxial), superlattices, and related complex systems. We predict the composition and superlattice-period dependence of the band offsets and interband transitions of InAs/GaAs systems on InP and GaAs substrates.

DOI: 10.1103/PhysRevB.66.045208 PACS number(s): 71.20.Nr, 71.15.−m

I. INTRODUCTION

InAs and GaAs are the building blocks of a diverse range of optoelectronic heterojunction systems, including (i) short-period superlattices $(InAs)_n/(GaAs)_m$ made of the binary constituents,[1–11] (ii) bulk $In_xGa_{1-x}As$ alloys,[12,13] (iii) epitaxial alloy films on InP, $In_xGa_{1-x}As/InP$,[14–16] and on GaAs, $In_xGa_{1-x}As/GaAs$,[17–20] as well as (iv) alloy quantum-wells[15,20] $(In_xGa_{1-x}As)_n/InP$ on InP and $(In_xGa_{1-x}As)_n/GaAs$ on GaAs, and (v) GaAs-embedded InAs quantum dots.[21–23] We wish to provide a uniform theoretical description of the electronic structure of such systems, (i)–(v), by using a single theoretical approach. By ''electronic structure'' we include the band gaps, interband transition energies and their dipole elements, wave functions localization, and strain-modified band offsets.

The current status of theoretical modeling of such systems is that different approaches are often used to describe different subsystems. For example, short-period superlattices made of *binary constituents* are often treated by atomistic approaches such as the local-density approximation (LDA),[24] tight binding,[25–27] or empirical-pseudopotential method (EPM),[28–32] yet, superlattices made of *alloy constituents* are deemed too complex to be treated by such methods, and are described instead via continuum effective-mass approximations (EMA), including single-band or few-band $k\cdot p$ methods.[33–35] The electronic structure of bulk alloys,[12,13] e.g., the optical bowing in $In_xGa_{1-x}As$, is rarely predicted theoretically, (see, however, Refs. 36–40 for the modern theory of alloy bowing). Instead one uses[33–35] the observed phenomenological bowing in modeling of alloy heterojunctions. Even when an atomistic theory of bowing in bulk alloys is attempted,[36–40] such descriptions are not extended to alloy *superlattices*, such as $(In_xGa_{1-x}As)_n/(InP)_m$, which represent a higher level of complexity. The use of different theoretical approaches with widely varying degrees of accuracy to describe the various InAs/GaAs subsystems can be problematic not only because of potential inconsistencies (and lack of elegance), but also because the ranges of applicability are currently unknown. For example, it is not obvious what are the minimum layer periods (n,m) of A_nB_m superlattices before the continuum EMA description starts to fail, thus requiring an atomistic description,[30–32] or when the difference in atomic potentials V_A-V_B between the alloy constituents is too large to justify a virtual-crystal description of the A_xB_{1-x} alloy, as is the case in $GaAs_xN_{1-x}$ alloys.[41,42]

The modern electronic structure theory of solids and molecules[43,44] delivers the basic electronic properties through an effective single-particle Schrödinger equation,

$$\left\{-\frac{1}{2}\nabla^2+V_{scr}(r)+\sum_n\sum_\alpha u_\alpha(\mathbf{r}-\mathbf{R}_n-\mathbf{d}_\alpha)\right\}\psi_i=\epsilon_i\psi_i(\mathbf{r}), \tag{1}$$

where u_α is an external atomic potential (e.g., ionic pseudopotential, or electron-ion $-Z/r$ field) of atom of type α = Ga, In, As located at lattice site $\mathbf{d}_\alpha$ within unit cell at $\mathbf{R}_n$, and $V_{scr}(r)$ is the screening response[45] of the system to such external potentials. (We consistently use lowercase symbols u,v to denote potentials of single atoms, whereas V denotes the potential of a set of atoms, e.g., an alloy, superlattice, or quantum dot.) The specification of the structure—superlattice or random alloy—is given by the collection of position vectors $\{\mathbf{R}_n;\mathbf{d}_\alpha\}$. While the $\{u_\alpha\}$ are properties of individual atoms, and are thus superposed linearly in Eq. (1), the screening $V_{scr}(r)$ is generally not linearly superposable. In the LDA (Ref. 45) it includes a linearly superposable interelectronic Coulomb term $V_H(\mathbf{r})$, as well as a nonlinear exchange and correlation term $V_{XC}(\mathbf{r})$. The total screening $V_{scr}=V_H+V_{XC}$ needs, in general, to be obtained self-consistently, and may even contain spatial nonlocality.[43,44] If, however, one considers physical systems made of a limited number of recurring chemical motifs, one could attempt to decompose the global screening into atomiclike components, thereby defining *screened potentials* v_α (Refs. 46–49) via

$$V=V_{scr}(r)+\sum_n\sum_\alpha u_\alpha(\mathbf{r}-\mathbf{R}_n-\mathbf{d}_\alpha)$$

$$\approx\sum_n\sum_\alpha v_\alpha(\mathbf{r}-\mathbf{R}_n-\mathbf{d}_\alpha). \tag{2}$$

The various InAs/GaAs systems discussed above (as well as other isovalent and isostructural semiconductor pairs) all involve five basic atomic tetrahedra As (Ga_pIn_{4-p}) with $0 \leqslant p \leqslant 4$, where the pure binaries InAs and GaAs, respectively, are $p=0$ and $p=4$, whereas mixed clusters have $p=1$, 2, and 3. Moreover, all of the systems we consider—alloys, superlattices, heterojunctions—have fully satisfied fourfold coordination without free surfaces, reconstructions, or broken bonds. Thus, we wondered if just a few screened potentials $\{v_\alpha\}$ could be constructed from some prototype systems, and then used in a transferable way to describe the full range of alloys, heterojunctions, and quantum dots via

$$\left\{ -\frac{1}{2}\nabla^2 + \sum_n \sum_\alpha v_\alpha(\mathbf{r}-\mathbf{R}_n-\mathbf{d}_\alpha) \right\} \psi_i = \epsilon_i \psi_i . \qquad (3)$$

Our current understanding of the nonlinear nature of the exchange-correlation screening[45] within $V_{scr}(\mathbf{r})$, and the positional nonlocality of the self-energy[44] suggests that Eq. (2) cannot hold universally for all eigenvalues $\{\epsilon_i\}$ of the Schrödinger equation (3), or for all structures (bulk as well as surface). Nevertheless, it is interesting to explore if this ansatz holds for a useful window of energy eigenvalues (e.g., a few eV around the band gap) and for a restricted rage of structures [e.g., systems made of As(Ga_pIn_{4-p}), without free surfaces or undercoordinated atoms]. If an accurate representation such as Eq. (2) does exist, so that the band structure, effective-mass, deformation potentials, and other relevant experimental properties can be reproduced within reasonable accuracy via Eq. (3), then we can deliver a uniform theoretical description of alloys, superlattices, quantum wells, and quantum dots within a single theoretical approach. This may be computationally feasible since, given such a potential, Eq. (3) can be solved even for a million atoms,[50,51] provided we restrict our attention to a fixed energy window around the fundamental band gap. We next summarize our experience in constructing an accurate pseudopotential v_α of the form needed in Eqs. (2) and (3).

II. OUR CURRENT EMPIRICAL PSEUDOPOTENTIALS

The traditional empirical pseudopotential,[46–49] designed for binary bulk semiconductors, used a plane-wave basis, where the Hamiltonian matrix for reciprocal lattice vectors $\mathbf{G}$ and $\mathbf{G}'$ was

$$H_{\mathbf{G},\mathbf{G}'} = \frac{1}{2}G^2\delta_{G,G'} + V(\mathbf{G}-\mathbf{G}'). \qquad (4)$$

The first term represents the kinetic energy, and the second term represents the Fourier transform of the screened pseudopotential [right-hand side of Eq. (2)]. Spin-orbit interactions, and other nonlocal terms can also be introduced.[49] Equation (2) and the Hamiltonian Eq. (4) are solved for the bulk solid by expanding the wave function in plane waves,

$$\Psi_{i,k}(r) = e^{i\underline{k}\cdot\underline{r}} \sum_G^{G_{max}} A_{k+G}^{(i)} e^{i\underline{G}\cdot\underline{r}}, \qquad (5)$$

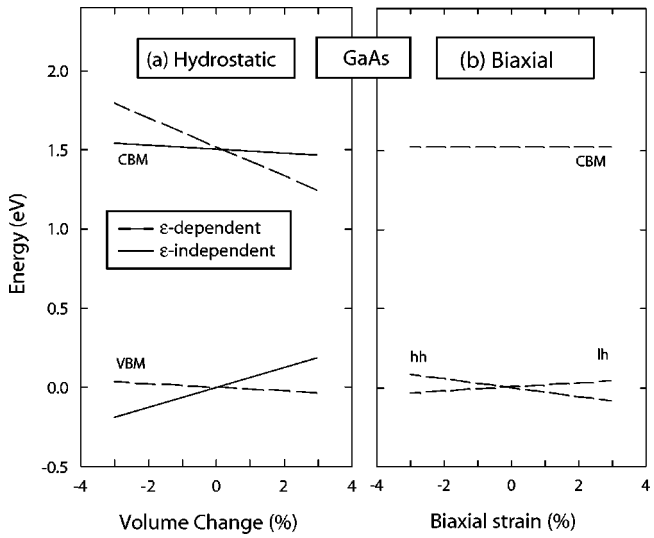

FIG. 1. GaAs band-edge energy dependence on (a) hydrostatic pressure, and (b) biaxial deformation, for strain independent and strain dependent empirical pseudopotentials. a_v and a_c denote the absolute valence (v) and conduction (c) deformation potentials. Solid lines denote the available strain independent data and dashed lines denote the explicitly strain dependent results.

where the highest momentum component G_{max} in the basis is determined by a cutoff energy,

$$\frac{1}{2}|G+k|^2 \leqslant E_{cut}. \qquad (6)$$

This type of empirical potential was constructed in the 1960s (Refs. 46,47) and subsequently improved via nonlocal terms in the 1970s.[49] This class of potential was fit to the bulk band structure of binary solids, producing good bulk reflectivity spectra. However, this class of potentials is not usable for our purposes involving quantum nanostructures. *First*, $V(\mathbf{G})$ was constructed[46–49] only at the reciprocal lattice vectors $\mathbf{G}_n$ of the binary bulk solids, whereas application to large unit cell materials requires $V(\mathbf{G})$ at many intermediate values. *Second*, the all-important band offsets between different materials (e.g., InAs and GaAs) were not fitted (not being required for bulk calculations), so nanostructure confinement energies cannot be reproduced. *Third*, upon examination[52] it was found that the traditional empirical pseudopotentials[47,49] gave very poor bulk effective masses, so quantum-size dependence of energies could not be reproduced. *Fourth*, the dependence of the valence-band maximum (VBM) and conduction band minimum (CBM) band-edge energies on hydrostatic potentials was discovered[52,53] often to have an incorrect sign. This problem is illustrated in Fig. 1(a) for GaAs, where the solid lines depict the volume dependence of the VBM and CBM energies as a function of volume, using conventional empirical pseudopotentials $V(\mathbf{G})$ that depend only on momentum. Using this description, we see that the VBM energies move to more negative values as the material is compressed hydrostatically, [i.e., $a_V = V\partial\epsilon_{vbm}/\partial V$ is positive], whereas the CBM energies are comparatively pressure independent. In contrast, accurate

LDA calculations[54,55] predict a *large negative* $a_c<0$ deformation potential for the CBM, and small deformation potentials a_v for the VBM.[56,57] These trends cannot be fit by empirical potentials that depend only on momentum.[52]

The four problems with conventional EPM thus make it unusable for nanostructures exhibiting quantum confinement and strain. We have therefore generalized the form of the EPM to remedy these problems. We describe these generalizations below.

A. Continuous q-space form of the potential

We chose a parametrized form of potential that is continuous in reciprocal space, permitting application to large unit cells and alloyed materials that require the potential at many q points. The analytic form adopted for the fit is

$$v(q)=a_0\frac{(q^2-a_1)}{[a_2e^{a_3q^2}-1]}, \tag{7}$$

where a_0–a_3 are the fitting parameters. This form is not only continuous in q space, but also specified at $q=0$, permitting fits to the all-important band offsets between materials.

B. Strain dependence of the potential

The problem illustrated in Fig. 1(a) results from the fact that when v_α depends on position only (or, equivalently, on momentum, q only) it cannot accurately represent the change in potential resulting from deformation. This is unlike a self-consistent description, where the charge redistribution resulting from a deformation is built directly into the screening potential V_{scr}. Since in our approach $v_\alpha(r)$ of Eq. (2) includes both screening effects and the ionic pseudopotential $u_\alpha(r)$, we must build the response to deformation directly into the screened potential $v_\alpha(r)$. Thus, we add an explicit strain (ϵ) dependent term,[58]

$$V(r)=\sum_{n\alpha} v_\alpha(|r-R_{n\alpha}|)[1+\delta v\,\alpha(\epsilon)]. \tag{8}$$

To linear order under an arbitrary strain ϵ_{ij}, the change δv_α can be expressed as

$$\delta v_\alpha(\epsilon)=\sum_{ij} a_{ij}\epsilon_{ij}. \tag{9}$$

The T_d symmetry of the zincblende structure requires $a_{xx}=a_{yy}=a_{zz}$, and that $a_{ij}=0$ for $i\neq j$. Thus,

$$\delta v_\alpha(\epsilon)\propto \mathrm{Tr}(\epsilon). \tag{10}$$

Then, our screened atomic pseudopotential takes the form

$$v_\alpha(q,\epsilon)=v_\alpha(q,0)[1+\gamma_\alpha \mathrm{Tr}(\epsilon)], \tag{11}$$

where γ_α is a fitting parameter. Appendix A and the figure therein describe how the $\mathrm{Tr}(\epsilon)$ term is calculated.

The dashed lines in Fig. 1 show the effect of adding the extra term to the pseudopotential. The changes in energy of the *individual* bands are thus made consistent with the predicted trends in LDA calculations[54,55] which are in broad agreement with the limited experimental data. The largest contribution to the band-gap deformation potential now originates from the deformation potential of the CBM, which is now strongly negative. Since $\mathrm{Tr}(\epsilon)=0$ at equilibrium, the band structure of the equilibrium bulk band structure remains unaltered. Furthermore, the crystal-field splitting under biaxial strain is also preserved when the volume is kept constant. This point is illustrated in Fig. 1(b), where biaxial strain is applied to bulk GaAs while keeping the volume constant. The EPM calculated heavy hole–light hole deformation potential reproduces the observed value of 1.52 eV.

C. Local environment dependence of the potential

To improve the transferability of the potential, we let it depend on its local chemical environment. For example, the potential $v_{As}^{(p)}(q,\epsilon)$ of the As atom depends on the number p of Ga and In atoms surrounding it in the Ga_pIn_{4-p} tetrahedron. A simple approximation

$$v_{As}[Ga_pIn_{4-p}As]=\frac{4-p}{4}v_{As}(InAs)+\frac{p}{4}v_{As}(GaAs) \tag{12}$$

is utilized.

D. Kinetic-energy scaling

Using the local strain dependence of Eq. (8) and the local environment dependence of Eq. (12) permits a good description of a range of relevant electronic properties. However, a further generalization of the EPM proved important for a good simultaneous fit of band gaps and effective masses: the kinetic energy in the single-particle equation was scaled

$$H\psi_i=\left\{-\frac{\beta}{2}\nabla^2+V(r)\right\}\psi=\epsilon_i\psi_i, \tag{13}$$

where β is the scaling constant.[58,59] The origin of this term is as follows. In an accurate description of the crystal band structure, such as the *GW* method,[44] a general, spatially nonlocal potential, $V(r,r')$, is needed to describe the self-energy term. In the absence of such a term the occupied band width of an inhomogeneous electron gas is too large compared to the exact many-body result. To a first approximation, however, the leading effects of this nonlocal potential, $V(r,r')$, can be represented by scaling the kinetic energy. This can be seen by Fourier transforming $V(r,r')$ in reciprocal space, q, then making a Taylor expansion of q about zero. We find that the introduction of such a kinetic-energy scaling, β permits an improved simultaneous fit of both the effective masses and energy gaps. In this study, we fit $\beta=1.23$ for both materials.

E. G-space smoothing of the wave functions

The eigenfunctions of the Hamiltonian, Eq. (4), are solved for the bulk solid by expanding Eq. (5) in plane waves. Typically we use a cutoff energy E_{cut} of 5 Ry, which corresponds to only $\approx$60 plane waves at the Γ point of a two-atom primitive cell of GaAs. As the lattice constant of the system is

varied, plane waves are added or subtracted, potentially significantly increasing or decreasing the flexibility of the basis set. In order to minimize this effect, we find it beneficial to apply a weighting function to the individual plane waves

$$w_G = \frac{\cos(\theta)+1}{2}, \tag{14}$$

$$\theta = \pi \frac{E_G - \nu E_{cut}}{(1-\nu)E_{cut}}, \tag{15}$$

where E_G is the kinetic energy of the plane wave $|G+k|^2/2$. We find $\nu = 0.8$ provides an improved fit to cell-shape dependent properties such as hydrostatic and biaxial deformation potentials and alloy properties of strongly lattice-mismatched systems, e.g., GaAsN.

F. Fitting to experimental and LDA results

The empirical potentials are fit to the best available experimental data.[60] Where data are not available, or unreliable, the best theoretical calculations are used to provide target fitting values. The potential fitting includes the following:

(i) The experimentally measured band energies.[60]

(ii) The experimentally determined effective masses.[60]

(iii) The experimentally measured hydrostatic deformation potentials a_g and biaxial deformation potentials b.[60]

(iv) The LDA-calculated[55] hydrostatic band-edge deformation potentials a_v and a_c. (Only the *difference* $a_c - a_v = a_g$ currently is accessible experimentally; the individual components are not.)

(v) The LDA-calculated,[61] unstrained valence-band offsets between different semiconductors.

(vi) The experimentally determined spin-orbit splitting of the valence band.[60]

The screened pseudopotential v_α contains a local part and a nonlocal, spin-orbit interaction part and is fit to the properties described above. The nonlocal part of the potential describes the spin-orbit interaction,

$$H_{so} = \sum_{n\alpha} \hat{V}^{so}_\alpha(R_{n\alpha}) \equiv \sum_{n\alpha} \sum_l V^{so}_{l,\alpha}(r - R_{n\alpha}) |l\rangle_{R_{n\alpha}} \mathbf{L}\cdot\mathbf{S} \langle l|_{R_{n\alpha}}, \tag{16}$$

where $|l\rangle_{R_{n\alpha}}$ is a projector of angular momentum l centered at $R_{n\alpha}$, $\mathbf{L}$ is the spatial angular momentum operator, $\mathbf{S}$ is the Dirac spin operator, and $V^{so}_{l,\alpha}(r)$ is a potential describing the spin-orbit (SO) interaction. We use a Gaussian, *p*-only potential for V^{so}, and evaluate Eq. (16) using the method described in Appendix B and Ref. 62.

The properties to which the InAs and GaAs pseudopotential parameters are fit are given in Table I. We see that unlike the LDA, here we accurately reproduce the bulk band gaps and effective masses. We emphasize that a significant difference in our parameter set to that used conventionally in *kp* studies[21,33,35] is our choice of a negative magnitude for the valence-band deformation potential, a_v, which we have obtained from FLAPW calculations.[54,55] The final EPM parameters are given in Table II.

TABLE I. Fitted bulk electronic properties for GaAs and InAs using the screened atomic pseudopotentials. The hydrostatic deformation potential of the band gap and Γ_{15v} levels are denoted by a_{gap} and $a_{\Gamma_{15v}}$. The biaxial deformation potential is denoted by b and the spin-orbit splittings at the Γ_{15v} and L_{1v} points are denoted by Δ_0 and Δ_1. The EPM calculated alloy bowing coefficient is 0.40 eV [see Fig. 6(a)], and the valence-band offsets on different substrates are given in Fig. 5.

Property	GaAs		InAs	
	EPM	Expt. (Ref. 60)	EPM	Expt. (Ref. 60)
E_{gap}	1.527	1.52	0.424	0.42
$E_{X_{5v}}$	−2.697	−2.96	−2.330	−2.40
$E_{X_{1c}}$	1.981	1.98	2.205	2.34
$E_{X_{3c}}$	2.52	2.50	2.719	2.54
$E_{L_{3v}}$	−1.01	−1.30	−5.76	−6.30
$E_{L_{1c}}$	2.36	1.81	1.668	1.71
m_e^*	0.066	0.067	0.024	0.023
$m^*_{hh}[100]$	0.342	0.40	0.385	0.35
$m^*_{hh}[111]$	0.866	0.57	0.994	0.85
$m^*_{lh}[100]$	0.093	0.082	0.030	0.026
a_{gap}	−7.88	−8.33	−6.79	−5.7
$a_{\Gamma_{15v}}$	−1.11	−1.0	−0.826	−1.0
b	−1.559	−1.7	−1.62	−1.7
Δ_0	0.34	0.34	0.36	0.38
Δ_1	0.177	0.22	0.26	0.27

Once we have the screened pseudopotentials, Eq. (3) can now be solved for the electronic structure for given $\{v_\alpha\}$ and $\{\mathbf{R}_n, \mathbf{d}_\alpha\}$ without additional approximations except those used to construct $\{v_\alpha\}$. This development is due to advances in fast ("order N") diagonalization methods[50,51] and the ease of exactly calculating the matrix elements of v_α in a basis of plane waves. In this approach all geometries (alloys, superlattices, quantum dots, and wires) and systems are treated equivalently, using a single input set $\{v_\alpha\}$. Thus, any discrepancy between predicted results and experimental results can be traced to some approximation in $\{v_\alpha\}$. Here we will describe the application of Eq. (3) to the electronic structure of various systems constructed from the InAs and GaAs building blocks. This approach provides a uniform, atomistic description of the electronic structure of such systems.

III. EQUILIBRIUM ATOMIC POSITIONS

A full calculation for an alloy, superlattice, or quantum dot requires two steps.

(a) Obtaining reliable equilibrium atomic positions for a *given* atomic configuration, [e.g., $(GaAs)_n/(InAs)_m$ (001) superlattice].

(b) Obtaining reliable electronic energy levels for this atomic configuration and atomic positions.

For (a), we will use a valence force field[63–66] fit to experiment. For (b), we will use a fast-diagonalization method[50,51] to solve the pseudopotential Schrödinger equation, Eq. (3), in the plane-wave basis of Eq. (5) and previously obtained empirical potentials.

TABLE II. Parameters of the InGaAs EPM used in this study. The potentials were fitted at a plane-wave cutoff of 5 Ry, with kinetic-energy rescaling $\beta=1.23$ and smoothing $\nu=0.8$. We denote the potential to be used for a Ga atom when bonded to an As atom as "Ga-As."

Species	a_0	a_1	a_2	a_3	γ	Spin Orbit
Ga-As	432960.04	1.7842354	18880.626	0.20809693	2.5639153	0.0460
As-Ga	10.938638	3.0904963	1.1039588	0.23304077	0.0	0.0976
In-As	644.12963	1.5126251	15.200855	0.35374034	2.1821453	0.4800
As-In	26.468192	3.0312950	1.2464169	0.42129203	0.0	0.0976

A. Equilibrium atomic positions in superlattices

1. Continuum elasticity (CE) theory for strained superlattices

A film of a material grown epitaxially on a thick substrate will strain so that its atoms grow in registry with those of the substrate. Thus, its dimension $a_{\parallel}$, the lattice parameter of the layer parallel to the interface, becomes equal to that of the substrate a_s (coherency condition), and $a_{\perp}$, the lattice parameter of the layer perpendicular to the interface, is determined by the strain tensor. Based on macroscopic continuum elasticity theory,[67–69]

$$a_{\perp}(a_s,\hat{G})=a_{eq}-[2-3q(\hat{G})](a_s-a_{eq}). \tag{17}$$

Here, $\hat{G}$ is the direction of deformation and the epitaxial strain reduction factor is given by

$$q(\hat{G})=1-\frac{B}{C_{11}+\gamma(\hat{G})\Delta}, \tag{18}$$

where B is the bulk modulus, the C_{ij} are elastic constants of the embedded material, and

$$\Delta=C_{44}-\frac{1}{2}(C_{11}-C_{12}) \tag{19}$$

is the elastic anisotropy. γ is a purely geometric factor given by

$$\gamma(\hat{G})=\gamma(\phi,\theta)=\sin^2(2\theta)+\sin^4(\theta)\sin^2(\phi), \tag{20}$$

where ϕ are θ the spherical angles formed by $\hat{G}$. A general expression for $q(\hat{G})$ is given in Ref. 67. Explicit expressions for $q(\hat{G})$ along the principal directions (001), (011), and (111) are

$$q[001]=\frac{2}{3}\left(1-\frac{C_{12}}{C_{11}}\right),$$

$$q[110]=\frac{1}{3}\,\frac{C_{11}-C_{12}+6C_{44}}{3C_{11}+C_{12}+2C_{44}},$$

$$q[111]=\frac{4C_{44}}{C_{11}+2C_{12}+4C_{44}}. \tag{21}$$

Thus, for the superlattice along the (001) direction the perpendicular strain $\epsilon_{\perp}=(a_{\perp}-a_{eq})/a_{eq}$ becomes

$$\epsilon_{\perp}^{(001)}=-2\frac{C_{12}}{C_{11}}\epsilon_{\parallel} \tag{22}$$

and for the superlattice along the (111) direction, it is

$$\epsilon_{\perp}^{(111)}=-\frac{2C_{11}+4C_{12}-4C_{44}}{C_{11}+2C_{12}+4C_{44}}\epsilon_{\parallel}. \tag{23}$$

2. Valence force field (VFF) method

Although the continuum elasticity theory gives good estimates of cell-external parameters for a supercell (e.g., the $a_{\perp}$ value), it does not give any information as to the positions and local strains of the atoms inside the supercell. To calculate the relaxed atomic positions within the supercell, we use a generalization (generalized VFF, GVFF) of the original[63] valence force field model. Our implementation of the VFF includes bond stretching, bond angle bending, and bond-length/bond-angle interaction terms in the VFF Hamiltonian. This enables us to accurately reproduce the C_{11}, C_{12}, and C_{44} elastic constants in a zinc blende bulk material.[60] We have also included higher order bond stretching terms, which give the correct dependence of the Young's modulus with pressure. The GVFF total energy can be expressed as

$$\begin{aligned}E_{VFF}=&\sum_i\sum_j^{nn_i}\frac{3}{8}[\alpha_{ij}^{(1)}\Delta d_{ij}^2+\alpha_{ij}^{(2)}\Delta d_{ij}^3]\\&+\sum_i\sum_{k>j}^{nn_i}\frac{3\beta_{jik}}{8d_{ij}^0d_{ik}^0}[(\mathbf{R}_j-\mathbf{R}_i)\cdot(\mathbf{R}_k-\mathbf{R}_i)\\&-\cos\theta_{jik}^0d_{ij}^0d_{ik}^0]^2+\sum_i\sum_{k>j}^{nn_i}\frac{3\sigma_{ijk}}{d_{ik}^0}\Delta d_{ij}[(\mathbf{R}_j\\&-\mathbf{R}_i)\cdot(\mathbf{R}_k-\mathbf{R}_i)-\cos\theta_{jik}^0d_{ij}^0d_{ik}^0],\end{aligned} \tag{24}$$

where $\Delta d_{ij}^2=\{[(R_i-R_j)^2-d_{ij}^{0\,2}]/d_{ij}^0\}^2$. Here $\mathbf{R}_i$ is the coordinate of atom i and d_{ij}^0 is the ideal (unrelaxed) bond distance between atom types of i and j. Also, θ_{jik}^0 is the ideal (unrelaxed) angle of the bond angle $j-i-k$. The Σ^{nn_i} denotes summation over the nearest neighbors of atom i. The bond stretching, bond angle bending, and bond-length/bond-angle interaction coefficients $\alpha_{ij}^{(1)}(\equiv\alpha)$, β_{jik}, σ_{jik} are related to the elastic constants in a pure zinc blende structure in the following way:

TABLE III. Input GVFF parameters α, β, σ to Eq. (24) and their resulting elastic constants C_{11}, C_{12}, and C_{44}.

	α	β (10^3 dyne/cm)	σ	$\alpha^{(2)}$	C_{11}	C_{12} (10^{11} dyne/cm^2)	C_{44}
GaAs	32.153	9.370	−4.099	−105	12.11	5.48	6.04
InAs	21.674	5.760	−5.753	−112	8.33	4.53	3.80

$$C_{11}+2C_{12}=\sqrt{\frac{3}{4d_0}}\,(3\alpha+\beta-6\sigma),$$

$$C_{11}-C_{12}=\sqrt{\frac{3}{d_0}}\beta,$$

$$C_{44}=\sqrt{\frac{3}{d_0}}\frac{[(\alpha+\beta)(\alpha\beta-\sigma^2)-2\sigma^3+2\alpha\beta\sigma]}{(\alpha+\beta+2\sigma)^2}. \quad (25)$$

The second-order bond stretching coefficient $\alpha^{(2)}$ is related to the pressure derivative of the Young's modulus by dB/dP, where $B=(C_{11}+2C_{12})/3$ is the Young's modulus. Note that in the standard[63] VFF the last terms of Eq. (24) are missing, so $\sigma=0$ in Eq. (25). Thus there were only *two* free parameters (α,β) and therefore three elastic constants could not, in general, be fit exactly. The GVFF parameters and the resulting elastic constants are shown in Table III for GaAs and InAs crystals. For an InGaAs alloy system, the bond angle and bond-length/bond-angle interaction parameters β, σ for the mixed cation Ga-As-In bond-angle are taken as the algebraic average of the In-As-In and Ga-As-Ga values. The ideal bond-angle θ^0_{jik} is 109° for the pure zinc blende crystal. However, to satisfy Vegard's law for the alloy volume, we find that it is necessary to use $\theta^0_{Ga\text{-}As\text{-}In}=110.5°$ for the cation mixed bond angle.

3. CE vs VFF for superlattices

We first compare the strain $\epsilon_\perp$ calculated with continuum elasticity and with VFF for InAs and GaAs monolayers on GaAs and InP substrates. We use the same elastic constants in both calculations (Table III). The results shown in Table IV demonstrate that continuum elasticity also works well for film thicknesses down to a single monolayer. It is of interest that Brandt *et al.*[8] suggested in 1992 that continuum elasticity fails at the monolayer limit. In 1994, accurate LDA calculations[65] showed that the calculated deformation agreed very well with that predicted by continuum elasticity. Better experiments in 1995 (Refs. 9,10) and 1998 (Ref. 11) have indeed revealed that the earlier[8] experiments were incorrect and that continuum elasticity is serviceable down to the monolayer limit.

TABLE IV. Comparison of perpendicular strain $\epsilon_\perp$ obtained for monolayer insertions of InAs in GaAs or InP using continuum elasticity (CE) and valence force field (VFF).

Superlattice	Direction	$\epsilon_\perp^{CE}$ (%)	$\epsilon_\perp^{VFF}$ (%)
$(InAs)_1(GaAs)_\infty$	(001)	7.27	7.27
$(InAs)_1(GaAs)_\infty$	(111)	3.81	3.77
$(GaAs)_1(InP)_\infty$	(001)	−3.45	−3.36
$(InAs)_1(InP)_\infty$	(001)	3.40	3.41
$(GaAs)_1(InP)_\infty$	(111)	−1.77	−1.77
$(InAs)_1(InP)_\infty$	(111)	1.78	1.73

We next compare CE and VFF for $(GaAs)_n(InAs)_m$ on (001) GaAs. Continuum elasticity predicts the following for the $c/a(=a_\perp/a_\parallel)$ ratio vs (n,m) for the $(GaAs)_n(InAs)_m$ superlattices on a GaAs substrate:

$$(GaAs)_n(InAs)_m\frac{c}{a}=1+\frac{ma_\perp^{InAs}}{(n+m)a_\parallel},$$

$$(GaAs)_1(InAs)_\infty\frac{c}{a}=\frac{a_\perp^{InAs}}{a_\parallel},$$

$$(GaAs)_\infty(InAs)_1\frac{c}{a}=1,$$

$$(GaAs)_\infty(InAs)_\infty\frac{c}{a}=\frac{1}{2}\left(1+\frac{a_\perp^{InAs}}{a_\parallel}\right).$$

These CE results are shown as solid lines in Fig. 2, whereas the VFF results are shown as filled symbols. We see that CE is reasonably accurate for the (001) direction and also for the (111) direction [Fig. 2(b)].

Finally, we compare CE and VFF results for $(GaAs)_n(InAs)_m$ on InP. Continuum elasticity predicts the following for the c/a ratio for $(GaAs)_n(InAs)_m$ superlattices on an InP substrate:

$$(GaAs)_n(InAs)_m\frac{c}{a}=\frac{na_\perp^{GaAs}+ma_\perp^{InAs}}{(n+m)a_\parallel},$$

$$(GaAs)_1(InAs)_\infty\frac{c}{a}=\frac{a_\perp^{InAs}}{a_\parallel},$$

$$(GaAs)_\infty(InAs)_1\frac{c}{a}=\frac{a_\perp^{GaAs}}{a_\parallel},$$

$$(GaAs)_\infty(InAs)_\infty\frac{c}{a}=\frac{a_\perp^{GaAs}+a_\perp^{InAs}}{2a_\parallel}.$$

Figures 2(c) and 2(d), respectively, show the normalized c/a values calculated with CE and VFF for $(GaAs)_n(InAs)_m$ superlattices along (001) and (111) directions on GaAs and InP substrates. The asymptotic values of c/a for $m\to\infty$ and n

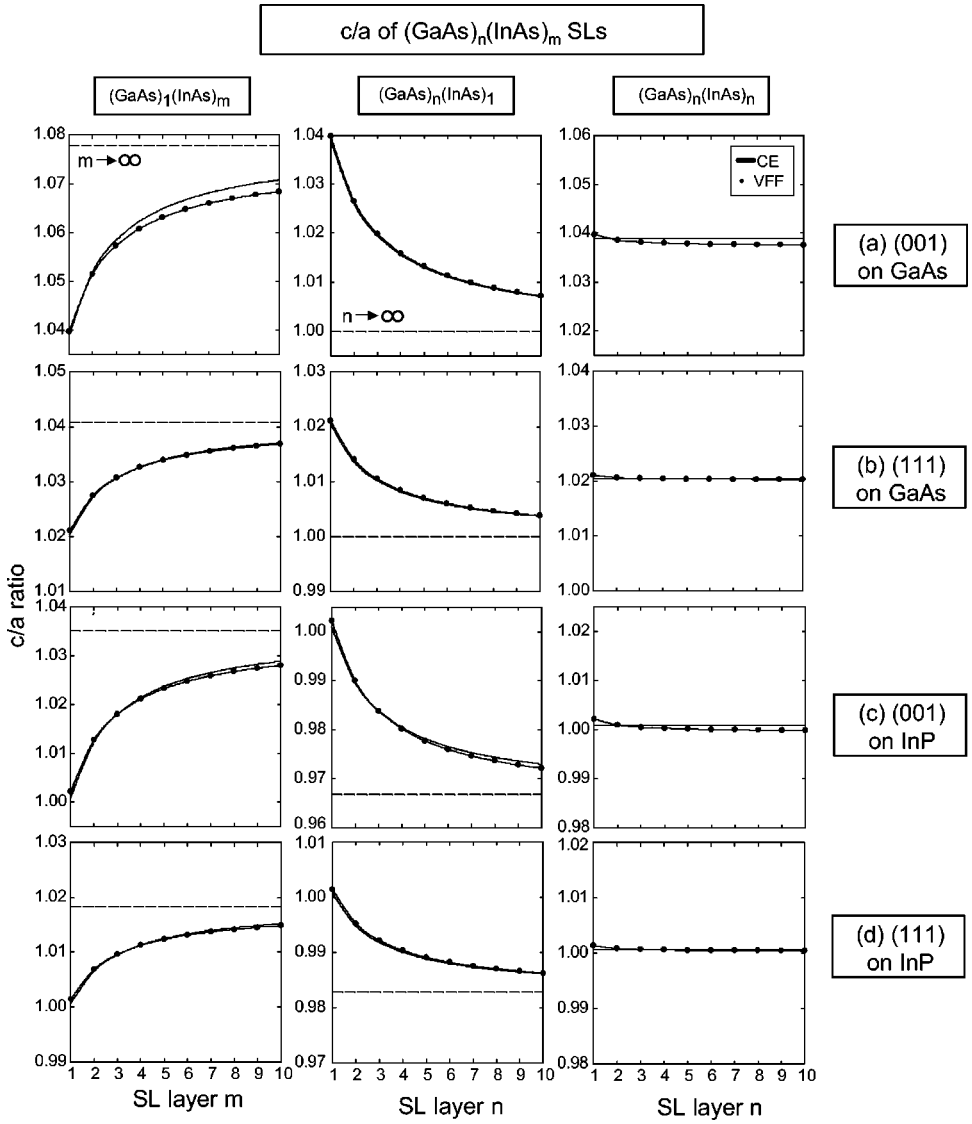

FIG. 2. c/a from continuum elasticity (CE) [solid lines, Eq. (17)] and from VFF (filled circles) for $(\mathrm{GaAs})_n(\mathrm{InAs})_m$ superlattices (a) along (001) and (b) (111) directions on GaAs, and (c) along (001) and (d) (111) directions on InP substrates. The asymptotic $n \rightarrow \infty$ values of c/a are shown as dashed lines.

$\rightarrow\infty$ are shown as dashed lines in Fig. 2. We see that continuum elasticity also works well for the c/a ratio.

4. VFF vs LDA for superlattices

As a simple test of our GVFF for alloy systems, we compared the relaxed atomic positions from GVFF with pseudopotential LDA results for a (100) $(\mathrm{GaAs})_1/(\mathrm{InAs})_1$ superlattice where the c/a ratio is fixed to 1, but we allow energy minimizing changes in the overall lattice constant (a_{eq}) and the atomic internal degrees of freedom (u_{eq}). We find

$$a_{eq}^{LDA} = 5.8612 \text{ Å},$$

$$u_{eq}^{LDA} = 0.2305,$$

while the GVFF results are

$$a_{eq}^{GVFF} = 5.8611 \text{ Å},$$

$$u_{eq}^{GVFF} = 0.2305.$$

A first-principles calculation by Bernard and Zunger[65] for $(\mathrm{InAs})_1(\mathrm{GaAs})_7$ (001) superlattice resulted in $\epsilon_\perp = 7.73\%$. Our GVFF gives 7.36%.

5. Atomic relaxation and interlayer spacing in InAs/GaAs superlattices

Figure 3 shows (001) and (111) interlayer distances in $(\mathrm{GaAs})_8/(\mathrm{InAs})_8$ superlattices. For an unrelaxed (001) superlattice, the internal coordinate z of the indium plane is 0.25 with respect to the c axis. The strain $\epsilon_\perp = (z - z_{equil})/z_{equil}$ is shown in Fig. 3. For an (111) superlattice, there are two internal coordinates, d_1 and d_2. The unrelaxed (ideal) values are $d_1 = \sqrt{3}/4$ and $d_2 = \sqrt{3}/12$. d_1 is the distance between Ga(In) and As atom layers where the bond is along (111) directions and d_2 is the distance between Ga(In) and As atom layers where the bond is along $(11\bar{1})$, $(1\bar{1}1)$, or $(\bar{1}11)$ directions. The strains $\epsilon_1 = (d_1 - d_{1,equil})/d_{1,equil}$ and $\epsilon_2 = (d_2 - d_{2,equil})/d_{2,equil}$ are shown in Fig. 3.

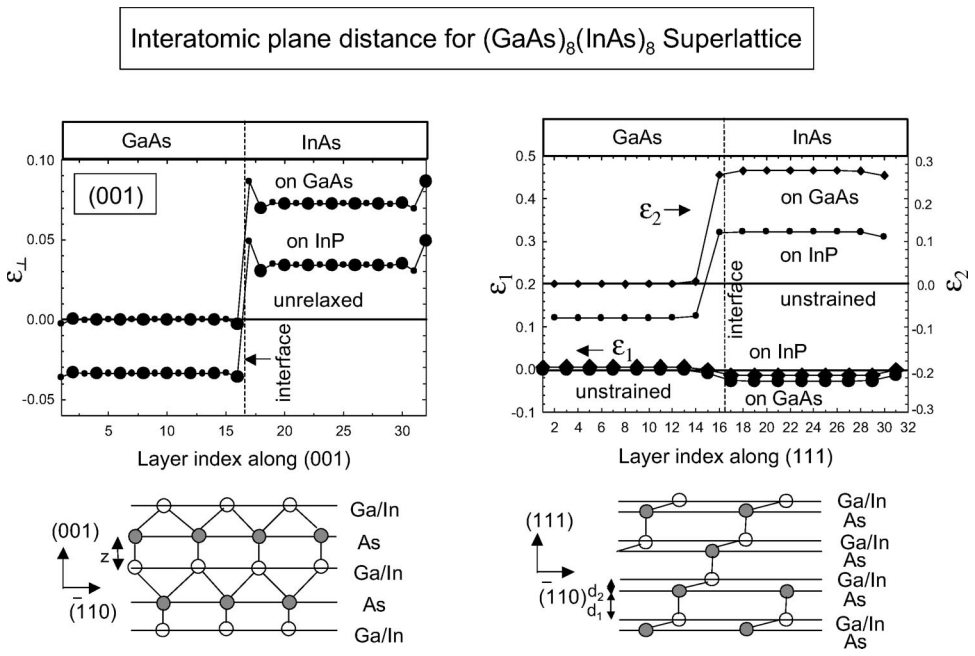

FIG. 3. (001) and (111) interlayer distances in $(GaAs)_8/(InAs)_8$ superlattices. d_1 is the distance between Ga(In) and As atom layers where the bond is along (111) directions and d_2 is the distance between Ga(In) and As atom layers where the bond is along $(11\bar{1})$, $(1\bar{1}1)$, and $(\bar{1}11)$ directions.

We see that on a GaAs substrate, the atoms of the GaAs segment of the superlattice (SL) are unrelaxed, whereas the strain in the InAs segment is positive. Most atoms have constant strain, except the atoms next to the interface. On the other hand, on an InP substrate, the GaAs segment is dilated ($\epsilon_\perp<0$) and the InAs segment is compressed ($\epsilon_\perp>0$), even though the lattice constant of the SL is almost matched to that of the substrate.

B. Equilibrium atomic positions in random alloys

The GVFF also is used to determine equilibrium atomic positions in random alloys. Here we create a supercell and randomly occupy cation sites with Ga and In atoms, according to the concentration $In_{1-x}Ga_xAs$. We then minimize the GVFF elastic energy by displacing atoms to their relaxed positions. We use a conjugate gradient algorithm using analytically calculated forces for both atomic positions and $a_\perp$. In a previous study[66] we reported the results for the closely related $In_{1-x}Ga_xP$ alloy, so we will not repeat the results for $In_{1-x}Ga_xAs$ here. In both cases we find a bimodal distribution of the nearest-neighbor anion-cation bond lengths, and a multimodal distribution of the cation-cation distances. Details are given in Ref. 66.

IV. STRAIN-MODIFIED BAND OFFSETS

Once we have determined the equilibrium atomic positions, and have a reliable screened pseudopotential, we can solve the Schrödinger equation, Eq. (3), in the plane-wave basis of Eq. (5). We first solve the simplest case, epitaxially deformed InAs and GaAs. Here, we imagine that GaAs is coherently strained on a substrate whose lattice constant a_s ranges from that of GaAs to that of InAs. The tetragonal deformation $a_\perp(a_s,\hat{G})$ in the perpendicular direction $\hat{G}$ is given by Eq. (17) if one uses continuum elasticity. We then solve the Schrödinger equation as a function of a_s. The resulting band edge energies $\epsilon_{vbm}(a_s,a_\perp)$ and $\epsilon_{cbm}(a_s,a_\perp)$ are shown on the right-hand side of Fig. 4. Similarly, when InAs is coherently compressed, we find the eigenvalues shown on the left-hand side of Fig. 4. The center panel aligns the unstrained valence-band maximum of GaAs and InAs using our LDA calculated band offset.[61] We see that expanding GaAs leads to an upward shift of the light-hole (lh) band, but a downward shift of the heavy-hole (hh) band. Compressing InAs leads, concomitantly, to an upward shift of hh, but in this case, lh also rises. The conduction-band minimum shifts to higher energies upon compression. Figure 4 also shows that the band offset depends sensitively on the substrate used. One can read from this figure the value of the

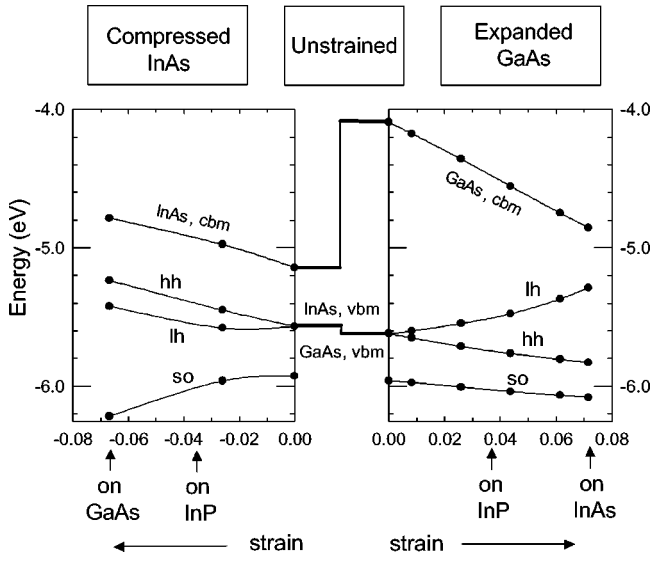

FIG. 4. The CBM and highest three VBM levels for strained binary GaAs and InAs calculated using the LDA values for the unstrained binaries (central panel), as well as the LDA deformation potentials. The lines represent the EPM fit.

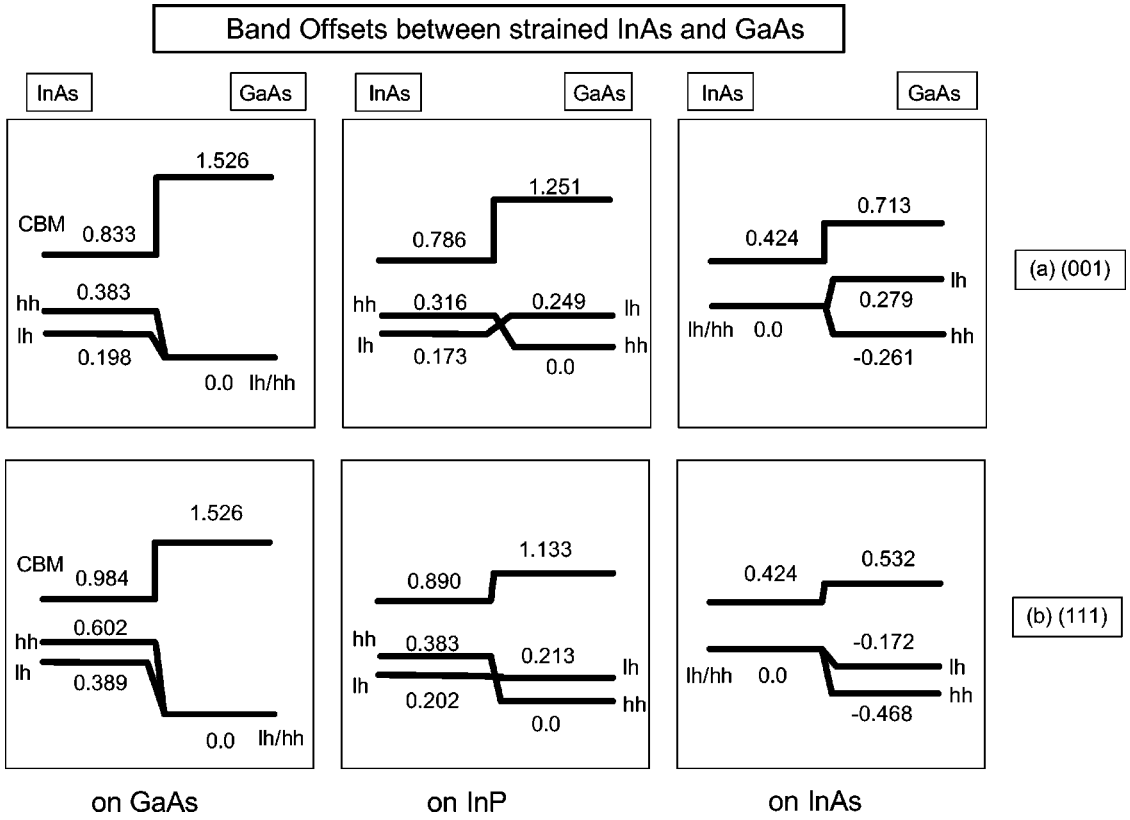

FIG. 5. Calculated strained band offsets of InAs/GaAs on various substrates and two layer orientations.

InAs/GaAs band offsets for various substrates such as GaAs, InP, and InAs. The calculated strained offsets on these substrates are given in Fig. 5 for two orientations, (001) and (111).

V. BAND-EDGE STATES IN RANDOM $In_xGa_{1-x}As$ ALLOYS

Figure 6 shows the band-edge states and the band gaps of (a) relaxed (''bulk'') $In_xGa_{1-x}As$ random alloys, and (b) epitaxial $In_xGa_{1-x}As$ alloys on GaAs and InP substrates, calculated using the empirical pseudopotential. For the calculation of the relaxed alloy we have used the Vegard lattice constant. For the epitaxial alloy the in-plane lattice constant is fixed and the perpendicular lattice constant $a_\perp$ is optimized. The bowing parameter is very small for the $In_xGa_{1-x}As$ alloys, being 0.4 eV for the bulk alloy, 0.0 eV for the alloy on GaAs, and -0.3 eV for the alloy on InP. The three highest valence-band states are shown in Fig. 6, i.e., light hole, heavy hole, and split off states. We note the following:

(i) *Epitaxy-induced reversal of bowing parameters*. The *bulk* alloy [Fig. 6(a)] shows a downward-bowing CBM and an upward-bowing VBM, with a total band-gap bowing coefficient $b_{gap}=b_c-b_v$ of $+0.4$ eV, in good agreement with experiment,[70,71] and with LDA calculations.[41]

The reason that E_v bows *upwards* with composition is that the highest valence states (anion p like, Γ_{8v}) are elevated by the lower-lying, Γ_{8v}-folding state $L_{4,5v}$, which is also anion p like.[72] On the other hand, E_c bows downwards with composition due to repulsion of the lowest conduction band (cation s like, Γ_{6c}) by higher lying L_{6c} and X_{6c} cation s-like states.[41,72] In contrast to the bulk alloys, however, the *epitaxial* alloys [Fig. 6(b)] show an *upward* bowing CBM ($b_c<0$), leading to a total band-gap bowing ≈ 0 eV on GaAs, -0.4 eV on InP, which is much smaller than that of the bulk alloy. The reason for this reversal is strain effects. When the alloy is *compressed* (e.g., In-rich $In_xGa_{1-x}As$/InP) its CBM and VBM both move up (much like in the zinc blende constituents, see Fig. 4) relative to the unstrained alloy. For InAs/InP these shifts are $+213$ meV and $+154$ meV, respectively. Conversely, when the alloy is *expanded* (e.g., Ga-rich $In_xGa_{1-x}As$/InP) its CBM moves *down* while the VBM moves *up*. For GaAs/InP these shifts are -390 meV and $+119$ meV, respectively. At the lattice-matched composition, $In_{0.53}Ga_{0.47}As$/InP, the CBM is unchanged. Due to the displacements of the In-rich and Ga-rich segments, the bowing (total, and for the CBM and VBM separately) changes sign via epitaxy.

(ii) *Hole localization*. The thin dashed horizontal line in Fig. 6(b) depicts the energy of the unstrained GaAs VBM. We see that the alloy hh energy is above the VBM of pure GaAs. Thus, the wave function would be localized on the *alloy* material, not on GaAs both in the bulk and in the epitaxial alloy on GaAs. However, at low In concentrations ($x_{In}<10\%$) the lh in the InGaAs/GaAs system has a very low offset with GaAs, so the hole is expected to be delocalized. For $x_{In}>10\%$, this hole is always localized on the In-rich material. For the epitaxial alloy on InP, we find a lh-hh

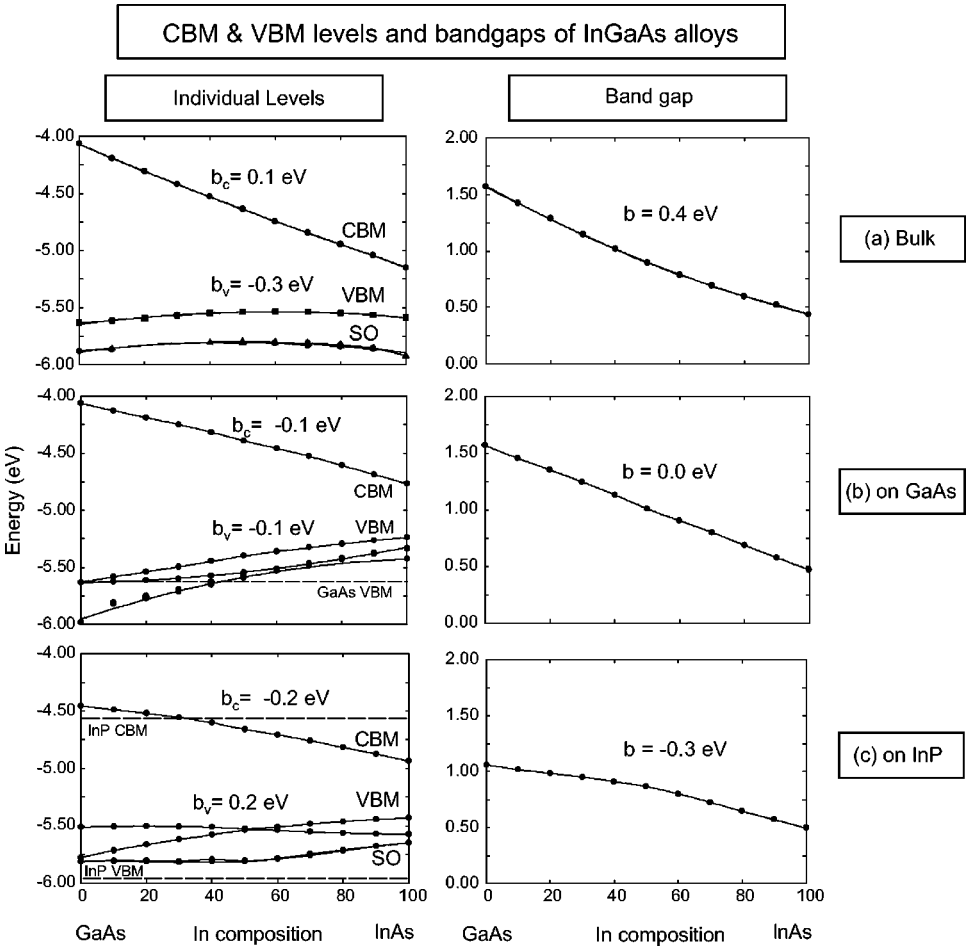

FIG. 6. Calculated band-edge states of InGaAs random alloys for (a) the "free-floating" bulk alloy, (b) the epitaxial alloy on GaAs, and (c) the epitaxial alloy on InP.

crossover[15] around 50% In, and a very shallow offset, suggesting rather delocalized holes.

(iii) *Electron localization*. In the bulk alloy and in the epitaxial alloy on GaAs the electrons always are localized on the In-rich material. The CBM of unstrained InP is shown as a dashed horizontal line in Fig. 6(c), exhibiting a crossover with the alloy CBM: for $x_{In}<30\%$ the electrons are localized on the InP substrate, whereas for $x_{In}>30\%$ they are localized on the alloy.[15]

VI. SHORT-PERIOD InAs/GaAs SUPERLATTICES

Figures 7, 8, and 9 show the CBM and VBM levels and band gaps for (001) and (111) $(GaAs)_n(InAs)_m$ superlattices on GaAs and InP. To understand the asymptotic results of the superlattice at $n\rightarrow\infty$ we have also calculated the energy levels of the epitaxial binary compounds InAs on InP, InAs on GaAs, GaAs on GaAs, and GaAs on InP. These levels are shown as a bar diagram to the right-hand side of each frame in Figs. 7, 8, and 9. Arrows connect energy levels in the superlattice with energy levels in the strained binary constituents, showing the limiting behavior. The epitaxial binaries were calculated by constraining each material to the substrate lattice constant and relaxing the atomic positions in the perpendicular direction. We see the following trends.

(i) For large n, the $(GaAs)_n(InAs)_1$ (Fig. 8) and $(GaAs)_1(InAs)_n$ (Fig. 9) levels becomes those of epitaxial GaAs (horizontal solid lines) and InAs (horizontal dashed lines), respectively.

(ii) The levels of $(GaAs)_n(InAs)_n$ (Fig. 7) go eventually to InAs levels but the convergence is slower. Since the effective mass of InAs is very small, it takes a very long period superlattice to localize the wave function within the cell. The localization of states is shown in Table V.

(iii) For (n,n) and $(1,n)$ superlattices, the highest VBM is for the (111) superlattice but the lowest CBM is for the (001) superlattice. For $(n,1)$ superlattice, it is the opposite, i.e. the highest VBM is for the (001) superlattice but the lowest CBM is for the (111) superlattice.

(iv) For the symmetric (n,n) SL, the CBM rises in energy, and the VBM moves down in energy as the period n decreases, as suggested by quantum confinement. On the other hand, these trends are reversed for the asymmetric $(n,1)$ SL (Fig. 8), where band-folding effects are greater than quantum-confinement effects. As a result, the band gap increases as n decreases in the (n,n) SLs, but in the $(n,1)$ SL the gap decreases.

(v) (111) superlattices have smaller gaps than (001) superlattices, as the former exhibit L folding that repels the Γ_{1c} CBM to lower energies more than the X folding, akin to (001) superlattices.[72]

Figure 10 shows the planar average of the wave functions

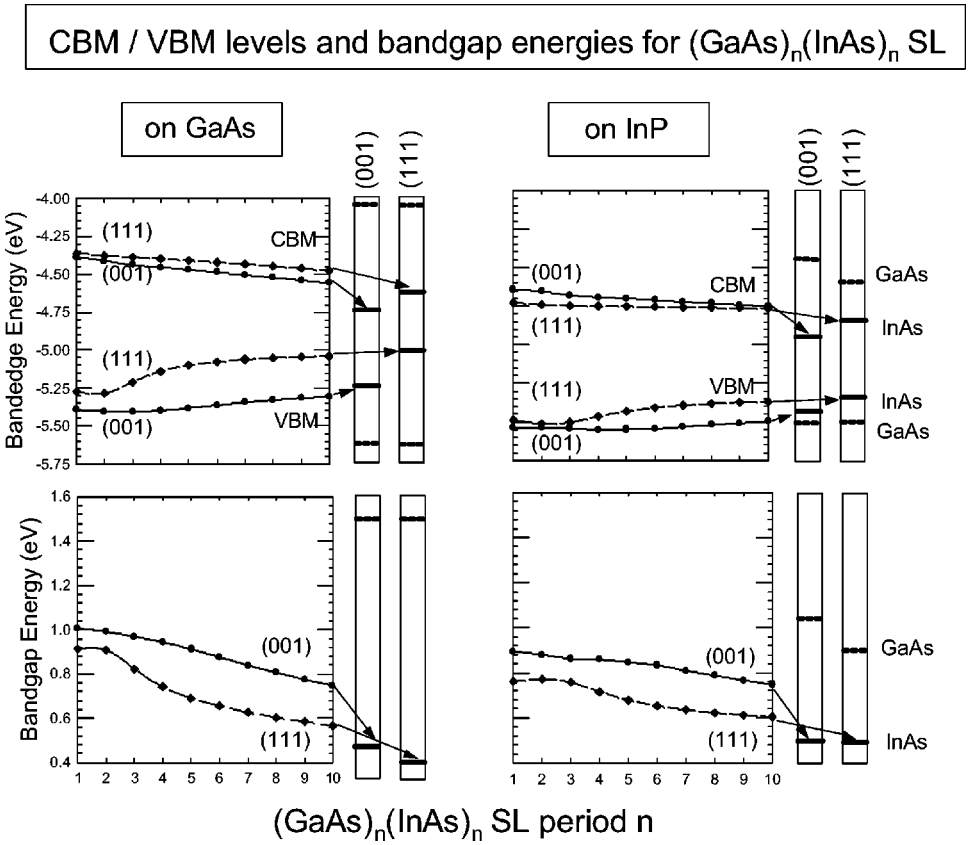

FIG. 7. The CBM and VBM levels for (001) and (111) $(GaAs)_n(InAs)_n$ superlattices on GaAs and InP. The boxes on the right-hand side of each panel depict the band edges of pure GaAs (dashed lines) and pure InAs (solid lines) binaries strained epitaxially on the corresponding substrate for the corresponding orientation. The two lower panels depict the band gaps.

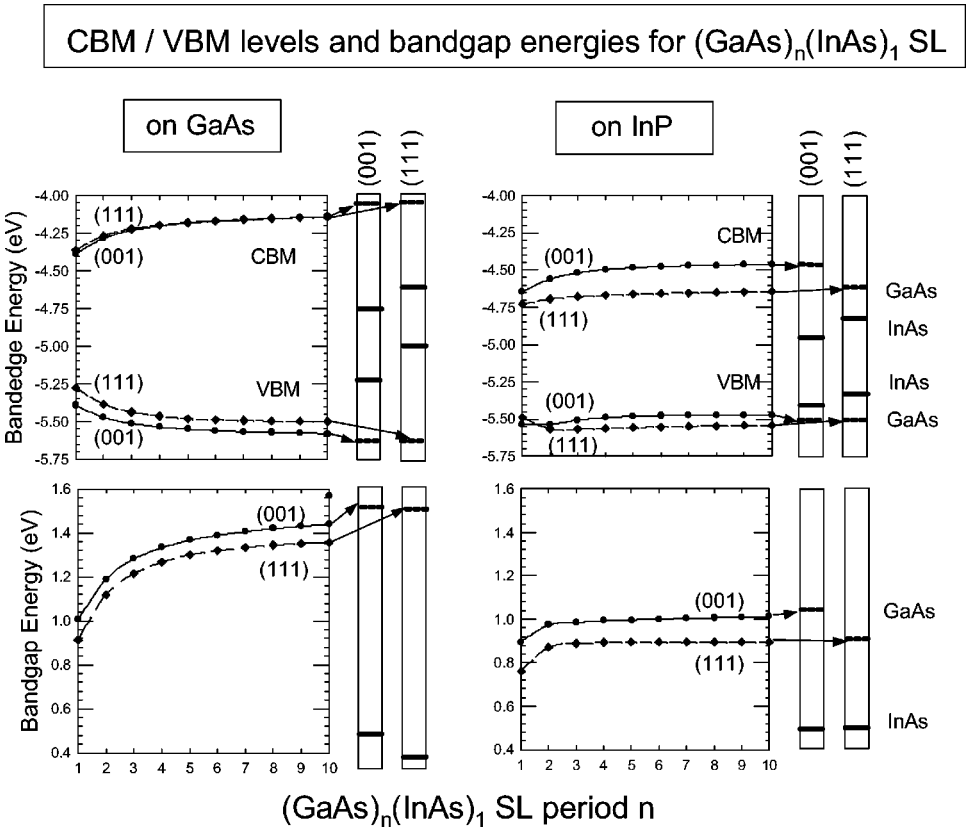

FIG. 8. The CBM and VBM levels and band gaps for (001) and (111) $(GaAs)_n(InAs)_1$ superlattices on GaAs and InP. The boxes on the right-hand side of each panel depict the band edges of pure GaAs and pure InAs binaries strained epitaxially on the corresponding substrate for the corresponding orientation.

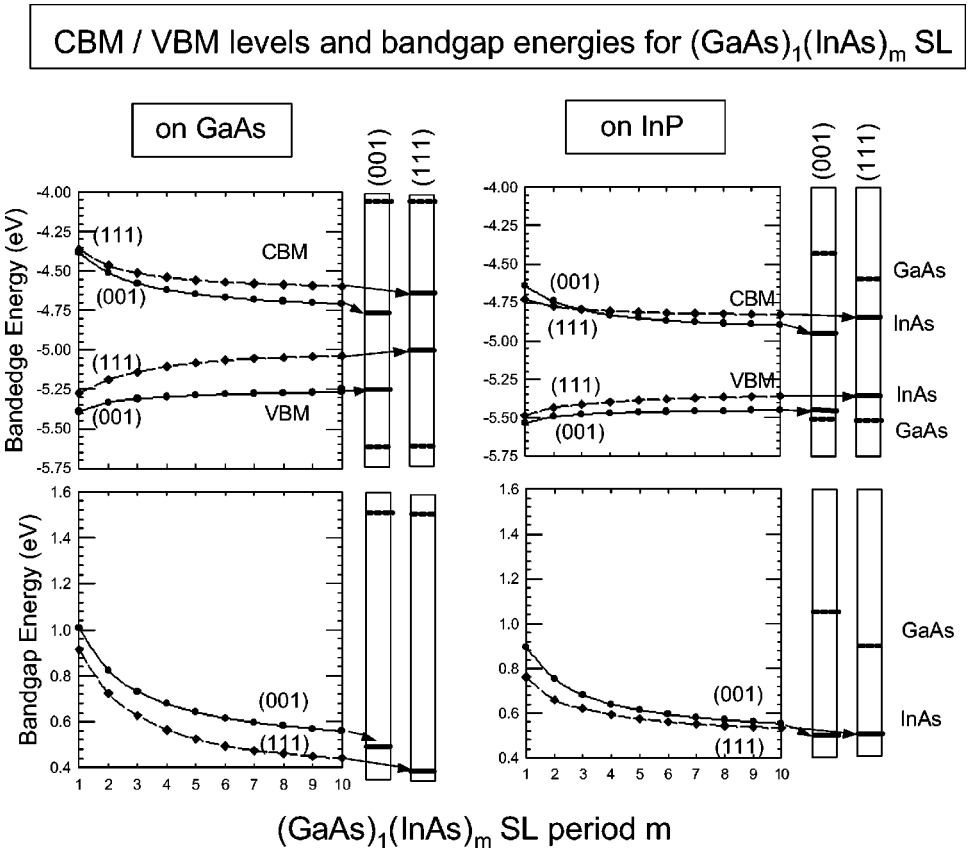

FIG. 9. The CBM and VBM levels and band gaps for (001) and (111) $(GaAs)_1(InAs)_m$ superlattices on GaAs and InP. The boxes on the right-hand side of each panel depict the band edges of pure GaAs and pure InAs binaries strained epitaxially on the corresponding substrate for the corresponding orientation.

of the (001) $(GaAs)_n(InAS)_n$ superlattice on InP for $n=2$, 6, and 10. For the largest period shown, $n=10$, the CBM states are localized on InAs, just as in the asymptotic behavior noted in Fig. 6. However, for shorter periods, Fig. 10 shows that the CBM is delocalized both on InAs and GaAs as predicted from first-principles calculations.[54] This shows that our EPM closely follows LDA calculations down to the monolayer regime.

As to the hole states, we see that for the largest period considered in Fig. 10 the lh1 state is rather delocalized with a preferred amplitude on GaAs. This reflects the small, <0.1 eV lh band offset on an InP substrate (Fig. 5). The asymptotic, $n\rightarrow\infty$ localization is on GaAs. On the other hand, the hh1 wave function is strongly localized on InAs, reflecting the larger hh offset of 0.32 eV for the InP substrate. The hh2 wave function is localized mostly on the interface.

Figure 11 depicts the calculated dipole matrix element squared for interband transitions. We see that the transition to the lowest electron state, $e1$, is polarized mostly in plane for $hh1\rightarrow e1$ and $so\rightarrow e1$ components, whereas for transitions from the lh1 level to $e1$, the strongest amplitude is for the out-of-plane transition. The dependence on superlattice period is rather weak.

TABLE V. Localization of states. Asterisks denote whether (001) or (111) orientation gives highest VBM or lowest CBM.

Superlattice	Substrate	Direction	VBM localized on	CBM localized on
(n,n)	GaAs	(001)	InAs	InAs*
(n,n)	GaAs	(111)	InAs*	InAs
(n,n)	InP	(001)	InAs	InAs*
(n,n)	InP	(111)	InAs*	InAs
$(n,1)$	GaAs	(001)	GaAs*	GaAs
$(n,1)$	GaAs	(111)	GaAs	GaAs*
$(n,1)$	InP	(001)	GaAs*	GaAs
$(n,1)$	InP	(111)	GaAs	GaAs*
$(1,n)$	GaAs	(001)	InAs	InAs*
$(1,n)$	GaAs	(111)	InAs*	InAs
$(1,n)$	InP	(001)	InAs	InAs*
$(1,n)$	InP	(111)	InAs*	InAs

VII. CONCLUSIONS

We find that an atomistic description of the electronic structure and a well-fit, modern empirical pseudopotential can deliver an accurate, detailed picture of random alloys, epitaxial alloys, superlattices, and quantum dots.[21] This approach does not suffer from the limitations of continuum effective-mass models, and can be applied to complex alloy systems of arbitrary geometry.

ACKNOWLEDGMENTS

This work was supported in part by Bettis Atomic Power Laboratory.

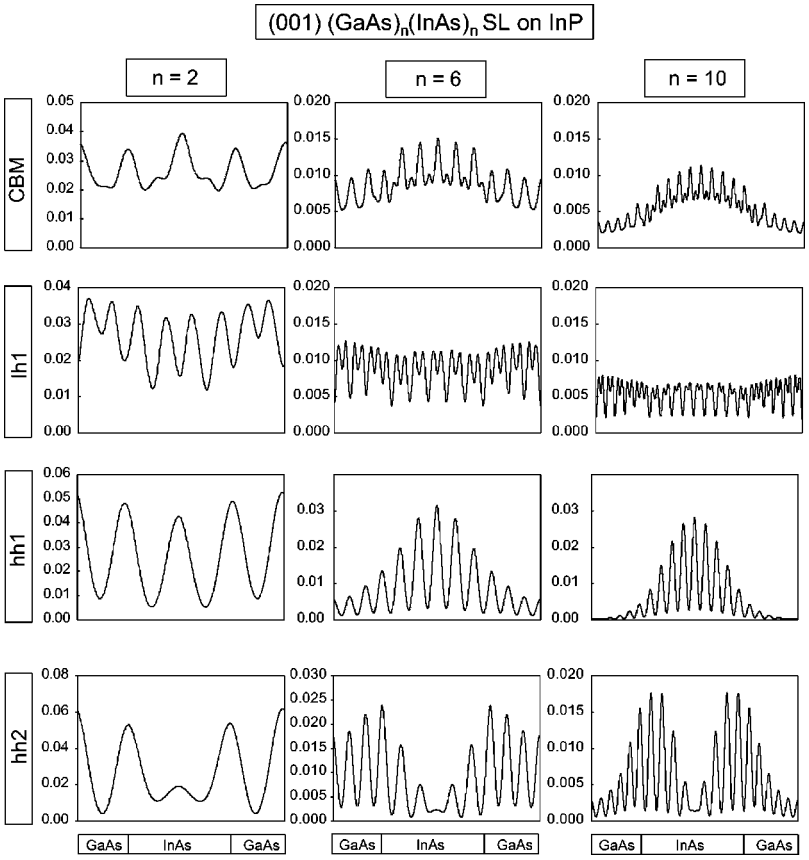

FIG. 10. The planar average of wave functions for (001) $(GaAs)_n(InAs)_n$ SL on InP for periods $n=2,6,10$ and for the states CBM, lh1, hh1, and hh2.

APPENDIX A: CALCULATION OF THE LOCAL STRAIN

To use the empirical pseudopotential, one needs a method to calculate the local strain for arbitrary systems. Figure 12 illustrates how the local strain is calculated. After the atomic positions are relaxed by minimizing the elastic energy, the local strain tensor ϵ_{ij} is calculated at each atomic site by considering the tetrahedron formed by the four nearest neighbor atoms. The distorted tetrahedron edges, $\mathbf{R}_{12}, \mathbf{R}_{23}$, and $\mathbf{R}_{34}$ are related to the ideal tetrahedron edges $\mathbf{R}^0_{12}, \mathbf{R}^0_{23}$, and $\mathbf{R}^0_{34}$ via which

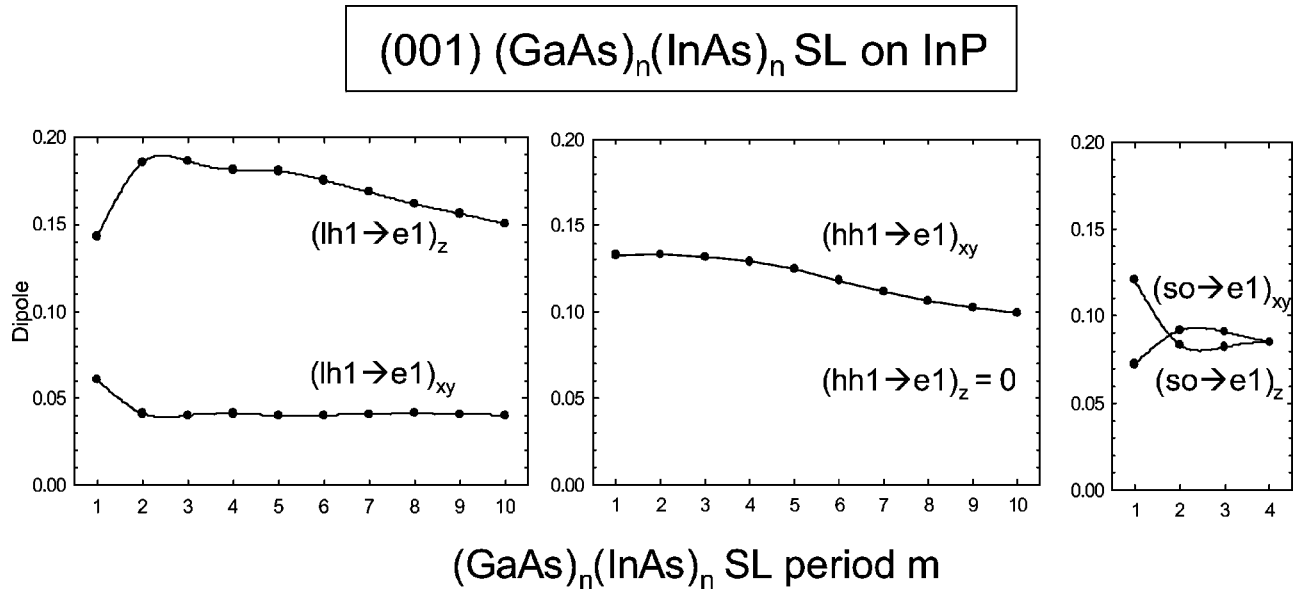

FIG. 11. The dipole elements for interband transitions in (001) $(GaAs)_n(InAs)_n$ SL on InP.

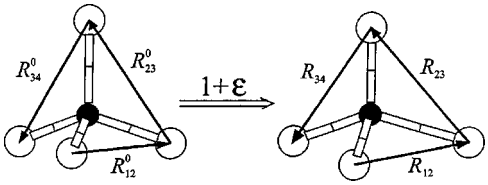

FIG. 12. Geometries of the atom centered tetrahedra used for calculation of the strain tensor.

$$\begin{pmatrix} R_{12,x} & R_{23,x} & R_{34,x} \\ R_{12,y} & R_{23,y} & R_{34,y} \\ R_{12,z} & R_{23,z} & R_{34,z} \end{pmatrix} = \begin{pmatrix} 1+\epsilon_{xx} & \epsilon_{yx} & \epsilon_{zx} \\ 1+\epsilon_{xy} & 1+\epsilon_{yy} & \epsilon_{zy} \\ \epsilon_{xz} & \epsilon_{yz} & 1+\epsilon_{zz} \end{pmatrix} \times \begin{pmatrix} R^0_{12,x} & R^0_{23,x} & R^0_{34,x} \\ R^0_{12,y} & R^0_{23,y} & R^0_{34,y} \\ R^0_{12,z} & R^0_{23,z} & R^0_{34,z} \end{pmatrix}. \quad \text{(A1)}$$

The ideal tetrahedron edges are $\{\mathbf{R}^0\}=\{[110]a/2,[0\bar{1}1]a/2,[\bar{1}10]a/2\}$, where a denotes the equilibrium lattice constant. The local strain, ϵ_{ij} is then calculated by a matrix inversion as

$$\begin{pmatrix} 1+\epsilon_{xx} & \epsilon_{yx} & \epsilon_{zx} \\ 1+\epsilon_{xy} & 1+\epsilon_{yy} & \epsilon_{zy} \\ \epsilon_{xz} & \epsilon_{yz} & 1+\epsilon_{zz} \end{pmatrix} = \begin{pmatrix} R_{12,x} & R_{23,x} & R_{34,x} \\ R_{12,y} & R_{23,y} & R_{34,y} \\ R_{12,z} & R_{23,z} & R_{34,z} \end{pmatrix} \begin{pmatrix} R^0_{12,x} & R^0_{23,x} & R^0_{34,x} \\ R^0_{12,y} & R^0_{23,y} & R^0_{34,y} \\ R^0_{12,z} & R^0_{23,z} & R^0_{34,z} \end{pmatrix}^{-1} - I, \quad \text{(A2)}$$

where I is the unit matrix.

Since only the trace of the strain is required, the evaluation of $\mathrm{Tr}(\epsilon)$ can be simplified as

$$\mathrm{Tr}(\epsilon)=\frac{\Delta V}{V}=\frac{(\mathbf{R}_{12}\times\mathbf{R}_{13})\dot{\mathbf{R}}_{14}/6}{V}-1, \quad \text{(A3)}$$

where V is the volume of the ideal, undistorted tetrahedron, i.e., $V=(\mathbf{R}^0_{12}\times\mathbf{R}^0_{13})\dot{\mathbf{R}}^0_{14}/6$.

APPENDIX B: CALCULATION OF THE SPIN-ORBIT INTERACTION

The spin-orbit interaction is included in the Hamiltonian via a nonlocal, atom-centered p-like potential. In order to maintain linear scaling with system size, we use the ''small box'' implementation of Ref. 62 to evaluate the potential.

The spin-orbit term in the Hamiltonian, Eq. (16), consists of finite-ranged, atom-centered potentials, assumed zero for $r \geqslant r_{cut}$. Only the part of ψ within r_{cut} has contributions to $\hat{V}_{SO}\psi(\mathbf{r})$, which leads to the following implementation. For a given atom at $\mathbf{R}_i$, on the real-space numerical grid, we consider a small box centered on $\mathbf{R}_i$. Defining $\psi_Q(\mathbf{r}) \equiv \psi(\mathbf{r})$ for grid points inside the small box Q, we then treat ψ_Q as if it were periodic within the small box. This permits us to use the fast Fourier transform of $\psi_Q(\mathbf{r})$, $\psi_Q(\mathbf{G}_Q)$, where $\mathbf{G}_Q$ is a reciprocal lattice vector of the small box Q. Now in Fourier space, we can directly evaluate the nonlocal spin-orbit potential, $v_Q(\mathbf{G}_Q,\mathbf{G}'_Q)$,

$$\phi_Q(\mathbf{G}_Q)=\sum_{\mathbf{G}'} v_Q(\mathbf{G}_Q,\mathbf{G}'_Q)\psi_Q(\mathbf{G}'_Q). \quad \text{(B1)}$$

Fourier transforming the new wave function ϕ_Q back to real space we then add this small box of wave function back to the full wave function. The computational effort for each atom is therefore fixed, independent of the total size of the system, and the cost of the method scales linearly with the size of the system.

For the spin-orbit potential itself, we adopt a Gaussian form, $v_p(r)=\exp[-(r/0.7)^2]$, and rescale the amplitude of this potential for different atoms.

[1] P. Voisin, M. Voos, J.Y. Marzin, M.C. Tamargo, R.W. Nahory, and A. Cho, Appl. Phys. Lett. **48**, 1476 (1986).

[2] M. Razeghi, P. Maurel, F. Omnes, and J. Nagel, Appl. Phys. Lett. **51**, 2216 (1987).

[3] H. Ohno, R. Katsumi, T. Takamu, and H. Hasegawu, Jpn. J. Appl. Phys. **24**, L682 (1985).

[4] T. Fukui and H. Saito, Jpn. J. Appl. Phys. **23**, L521 (1984).

[5] M.A. Tischler, N.G. Anderson, and S.M. Bedair, Appl. Phys. Lett. **49**, 1199 (1986).

[6] M.A. Tischler, N.G. Anderson, and S.M. Bedair, Appl. Phys. Lett. **50**, 1266 (1987).

[7] J.M. Gereard and J.Y. Marzin, Appl. Phys. Lett. **53**, 568 (1988).

[8] O. Brandt, K. Ploog, L. Tapfer, M. Hohenstein, R. Bierwolf, and F. Phillipp, Phys. Rev. B **45**, 8443 (1992).

[9] J.C. Woicik, K.E. Miyano, J.G. Pellegrino, P. Shaw, S.H. Southworth, and B.A. Karlin, Appl. Phys. Lett. **68**, 3010 (1996).

[10] J.C. Woicik, J.G. Pellegrino, S.H. Southworth, P.S. Shaw, B.A. Karlin, C.E. Bouldin, and K.E. Miyano, Phys. Rev. B **52**, 2281 (1995).

[11] Y. Zheng, J.C. Bouillard, B. Capelle, A. Lifchitz, and S. Lagomarsino, Europhys. Lett. **41**, 623 (1998).

[12] J. C. Woolley, in *Compound Semiconductors*, edited by R. K. Willardson and H. L. Goering (Reinhold, New York, 1962).

[13] P. Bhattacharya, *Properties of Indium Gallium Arsenide* (Inspen, Exeter, 1993), No. 8.

[14] J. Dalfors, T. Lundstrom, P.O. Holtz, H.H. Rudamson, B. Monamar, J. Wallin, and G. Lundgren, Appl. Phys. Lett. **71**, 503 (1997).

[15] D. Gershoni and H. Temkin, J. Lumin. **44**, 381 (1989).

[16] S.R. Forrest, P.H. Smith, R.B. Wilson, and H.L. Kaplan, Appl. Phys. Lett. **45**, 1199 (1984).

[17] J. Menendez, A. Pinczuk, D. Werder, S.K. Sputz, R.C. Miller, D.L. Sivco, and A.Y. Cho, Phys. Rev. B **36**, 8165 (1987).

[18] G. Ji, U.K. Reddy, D. Huang, T.S. Henderson, and H. Morkoc,

Superlattices Microstruct. **3**, 539 (1987).
[19] S.H. Pan, H. Shen, Z. Hany, F.H. Pollak, W. Zhuang, Q. Xu, A.P. Roth, R.A. Masut, C. Lacelle, and D. Morris, Phys. Rev. B **38**, 3375 (1988).
[20] J.Y. Marzin and E.V.K. Rao, Appl. Phys. Lett. **43**, 560 (1983).
[21] A. Zunger, MRS Bull. **23**, 35 (1998).
[22] M. Grundmann, D. Biemberg, and N. N. Ledentson, *Quantum Dot Heterostructures* (Wiley, New York, 1998).
[23] T. Lundstrom, W.V. Schoenfeld, H. Lee, and P.M. Petroff, Science **286**, 2312 (1999).
[24] R.G. Dandrea and A. Zunger, Phys. Rev. B **43**, 8962 (1991).
[25] D.L. Smith and C. Mailhiot, Rev. Mod. Phys. **62**, 173 (1990).
[26] Y.C. Chang and J.N. Schulman, Appl. Phys. Lett. **43**, 536 (1983).
[27] L.J. Sham and Y.T. Lu, J. Lumin. **44**, 207 (1989).
[28] G. Edwards and J.C. Inkson, Solid State Commun. **89**, 595 (1994).
[29] K.A. Mader and A. Zunger, Phys. Rev. B **50**, 17 393 (1995).
[30] D.M. Wood and A. Zunger, Phys. Rev. B **53**, 7949 (1996).
[31] L.W. Wang, S.H. Wei, T. Mattila, A. Zunger, I. Vurgaftman, and J.R. Meyer, Phys. Rev. B **60**, 5590 (1999).
[32] R. Magri, L.W. Wang, A. Zunger, I. Vurgaftman, and J.R. Meyer, Phys. Rev. B **61**, 10 235 (2000).
[33] D. Gershoni, C.H. Henry, and G.A. Baraff, IEEE J. Quantum Electron. **29**, 2433 (1993).
[34] M.G. Burt, J. Phys. C **4**, 6651 (1992).
[35] L.R. Ram-Mohan, K.H. Yoo, and R.L. Aggarwal, Phys. Rev. B **38**, 6151 (1988).
[36] A. B. Chen and A. Sher, *Semiconductor Alloys* (Plenum, New York, 1995).
[37] A. Zunger, S.-H. Wei, L.G. Ferreira, and J. Bernard, Phys. Rev. Lett. **65**, 353 (1990).
[38] J.E. Bernard and A. Zunger, Phys. Rev. B **36**, 3199 (1987).
[39] R. Magri, S. Froyen, and A. Zunger, Phys. Rev. B **44**, 7947 (1991).
[40] S.-H. Wei and A. Zunger, Phys. Rev. B **43**, 1662 (1991).
[41] S.-H. Wei and A. Zunger, Phys. Rev. Lett. **76**, 664 (1996).
[42] P.R.C. Kent and A. Zunger, Phys. Rev. Lett. **86**, 2613 (2001).
[43] *Electronic Density Functional Theory*, edited by J. F. Dobson, G. Vignale, and M. P. Das (Plenum, New York, 1996).
[44] L. Hedin, J. Phys. C **11**, 489 (1999).
[45] P. Hohenberg and W. Kohn, Phys. Rev. **136**, 864 (1964).
[46] D. Brust and J.C. Phillips, Phys. Rev. Lett. **9**, 389 (1962).
[47] M.L. Cohen and T.K. Bergstresser, Phys. Rev. **141**, 789 (1966).
[48] M. L. Cohen and V. Heine, in *Solid State Physics*, edited by H. Ehrenreich, F. Seitz, and D. Turnbull (Academic, New York, 1970), Vol. 24, p. 64.
[49] J.R. Chelikowsky and M.L. Cohen, Phys. Rev. B **10**, 5095 (1974).
[50] L.W. Wang and A. Zunger, J. Chem. Phys. **100**, 2394 (1994).
[51] A. Zunger, Phys. Status Solidi A **224**, 727 (2001).
[52] A. Williamson, J. Kim, L.W. Wang, S.H. Wei, and A. Zunger (unpublished).
[53] K.J. Chang, S. Froyen, and M.L. Cohen, Solid State Commun. **50**, 105 (1984).
[54] A. Franceschetti, S.H. Wei, and A. Zunger, Phys. Rev. B **50**, 17 797 (1994).
[55] S.-H. Wei and A. Zunger, Phys. Rev. B **60**, 5404 (1999).
[56] C.G. Van de Walle, Phys. Rev. B **39**, 1871 (1989).
[57] Many previous studies have drawn the deformation potentials of the VBM (a_v) from the ''model solid theory'' of Van de Walle.[56] However, more accurate LDA calculations[54,55] show that due to cation *d* and anion *p* coupling, a_v are *negative* for Ga and In compounds, i.e., $a_v = -0.58, -1.21, -1.32, -0.41, -1.00, -1.24$ eV for GaP, GaAs, GaSb, InP, InAs, InSb, respectively, meaning that as volume is compressed, the VBM energy moves upwards. In contrast, the ''model solid theory'' neglects implicit *p-d* coupling, thus, we find $a_v = +1.70, +1.16, +0.79, +1.27, +1.00, +0.36$ eV for GaP, GaAs, GaSb, InP, InAs, InSb, respectively.
[58] J. Kim, L.W. Wang, and A. Zunger, Phys. Rev. B **57**, 9408 (1998).
[59] A.J. Williamson and A. Zunger, Phys. Rev. B **61**, 1978 (2000).
[60] *Numerical Data and Functional Relationships in Science and Technology*, edited by Landolt-Börnstein (Springer-Verlag, Berlin, 1987), Vol. 22a.
[61] S.-H. Wei and A. Zunger, Appl. Phys. Lett. **72**, 2011 (1998).
[62] L.-W. Wang and A. Zunger, Phys. Rev. B **51**, 17 398 (1995).
[63] P. Keating, Phys. Rev. B **145**, 637 (1966).
[64] J.L. Martins and A. Zunger, Phys. Rev. B **30**, 6217 (1984).
[65] J.E. Bernard and A. Zunger, Appl. Phys. Lett. **65**, 165 (1994).
[66] A. Silverman, A. Zunger, R. Kalish, and J. Adler, Phys. Rev. B **51**, 10 795 (1995).
[67] A. Zunger, in *Handbook of Crystal Growth*, edited by D. T. J. Hurle (Elsevier, Amsterdam, 1994), Vol. 3, p. 998.
[68] V. Ozolins, C. Wolverton, and A. Zunger, Phys. Rev. B **57**, 4816 (1998).
[69] V. Ozolins, C. Wolverton, and A. Zunger, Appl. Phys. Lett. **72**, 427 (1998).
[70] S. Paul, J.B. Roy, and P.K. Basu, J. Appl. Phys. **69**, 827 (1991).
[71] J.R. Jensen, J.M. Hvam, and W. Langbein, J. Appl. Phys. **86**, 2584 (1999).
[72] S.H. Wei and A. Zunger, Phys. Rev. B **39**, 3279 (1989).